Journal of Biomedical Optics 5(2), 163–172 (April 2000)

Photon migration through fetal head *in utero* using continuous wave, near-infrared spectroscopy: development and evaluation of experimental and numerical models

Gargi Vishnoi
University of Pennsylvania
Department of Biochemistry and Biophysics
Philadelphia, Pennsylvania 19104

Andreas H. Hielscher*
State University of New York
Downstate Medical Center
Department of Pathology
Brooklyn, New York 11023

Nirmala Ramanujam
Britton Chance
University of Pennsylvania
Department of Biochemistry and Biophysics
Philadelphia, Pennsylvania 19104

Abstract. In this work experimental tissue phantoms and numerical models were developed to estimate photon migration through the fetal head *in utero*. The tissue phantoms incorporate a fetal head within an amniotic fluid sac surrounded by a maternal tissue layer. A continuous wave, dual-wavelength ($\lambda = 760$ and 850 nm) spectrometer was employed to make near-infrared measurements on the tissue phantoms for various source-detector separations, fetal-head positions, and fetal-head optical properties. In addition, numerical simulations of photon propagation were performed with finite-difference algorithms that provide solutions to the equation of radiative transfer as well as the diffusion equation. The simulations were compared with measurements on tissue phantoms to determine the best numerical model to describe photon migration through the fetal head *in utero*. Evaluation of the results indicates that tissue phantoms in which the contact between fetal head and uterine wall is uniform best simulates the fetal head *in utero* for near-term pregnancies. Furthermore, we found that maximum sensitivity to the head can be achieved if the source of the probe is positioned directly above the fetal head. By optimizing the source-detector separation, the signal originating from photons that have traveled through the fetal head can drastically be increased. [S1083-3668(00)01402-7]

Keywords: near-infrared spectroscopy; photon migration; trans-abdominal; *in utero*; cerebral blood oxygenation; tissue phantoms; finite-difference simulations; transport equation; diffusion equation; photon fluence; visiting probability.

Paper JBO-42010 received Sep. 3, 1999; revised manuscript received Mar. 2, 2000; accepted for publication Mar. 3, 2000.

1 Introduction

Noninvasive *ante partum* tests have been employed to assess fetal health for a long time now. These tests include *ante partum* electronic fetal heart rate monitoring, either alone as the nonstress test (NST) or as a part of the biophysical profile (BPP), which includes serial ultrasonographic examinations.[1–3] These tests provide an indirect measurement of fetal cerebral hemodynamics and oxygenation NST can forecast severe fetal jeopardy, but a high rate of false–positive *ante partum* assessment tests (75%–90% for the nonstress test and 20%–75% for the biophysical profile) have been reported.[4,5] This dilemma necessitates the need to reduce the false–positive rate of current *ante partum* assessment tests for the detection of fetal neurological compromise *in utero*.

Noninvasive, fast, trans-abdominal, near-infrared (NIR) spectroscopy of fetal cerebral blood oxygenation *in utero* may potentially avoid the pitfalls of current *ante partum* assessment tests. The customization of the well-established NIR technology[6–14] for this particular application could potentially represent a significant advance in perinatal care and NIR spectroscopy of large, deeply buried organs in the human body.

In the companion manuscript,[15] we studied the optical properties and physical geometry of maternal and fetal-head tissues *in utero* using clinical studies on the maternal abdomen and experimental studies on laboratory tissue phantoms. Specifically, a continuous wave (cw) spectrometer was modified and employed to simultaneously make NIR measurements at 760 and 850 nm, at a large (10 cm) and small (2.5/4 cm) source-detector separation, on the maternal abdomen, directly above the fetal head. A total of 19 patients were evaluated, whose average gestational age was 37 weeks ± 3. The average depth of the fetal head was 2.25 cm ± 0.7. At the large source-detector separation, the photons are expected to migrate through both the maternal and fetal tissues before being detected at the surface, while at the short source-detector separation, the photons are expected to migrate primarily through the superficial maternal tissues before being detected. Similar NIR measurements were made on laboratory

*Address all correspondence to Andreas H. Hielscher. Tel: 718-270-4562; Fax: 718-270-3313; E-mail: ahielscher@netmail.hscbklyn.edu

1083-3668/2000/$15.00 © 2000 SPIE

tissue phantoms, with variable optical properties and physical geometries. The optical properties were varied and obtained using different concentrations of India ink and intralipid in water, while the variable physical geometries were realized by employing glass containers of different shapes and sizes. The NIR measurements, made on the laboratory tissue phantoms, were compared to the NIR measurements made on the maternal abdomen. The results of the comparison were used to provide insight into the optical properties and physical geometry of the maternal and fetal tissues in the photon migration path through the fetal head *in utero*.

The goal of the current work is to develop and evaluate experimental tissue phantoms and theoretical models to estimate NIR photon migration through the fetal head *in utero* for various source-detector separations, fetal head positions, and fetal head optical properties. The tissue phantom should be complex enough to be congruent with the major clinical findings, yet simple enough to allow easy manipulation of various tissue and geometry parameters to obtain insight into the major factors influencing NIR measurements of the fetal head *in utero*. Various tissue phantoms were chosen and a dual wavelength, cw spectrometer was employed to make NIR measurements on these phantoms. Next, the NIR measurements on the laboratory tissue phantoms were compared to numerical, finite-difference simulations that provide solutions to the diffusion as well as the transport equation. This comparison was made to determine which numerical model best describes photon migration through the tissue phantom. Finally, the optimal numerical model was employed to estimate photon migration through the fetal head *in utero* for various source-detector separations, fetal head positions, and fetal head optical properties. Evaluation of the results indicates that these experimental and theoretical models are useful for assessing the accuracy and sensitivity of trans-abdominal, NIR spectroscopy for measuring and quantifying fetal cerebral blood saturation *in utero*.

In the following section, a detailed description of the experimental and theoretical models is provided. This is followed by a presentation of the NIR measurements on the laboratory tissue phantoms and results of simulations based on the diffusion and transport equations. Finally, the effects of various source-detector separations, fetal head positions, and fetal head optical properties on photon migration through the fetal head *in utero* are discussed.

2 Materials and Methods

2.1 Instrumentation

A dual wavelength, cw, NIR spectrometer was employed in this investigation and is described in detail in the companion manuscript.[15] This instrument incorporates halogen and tungsten light sources, a pair of silicon photodetectors, filtered at 760 and 850 nm, respectively, an analog differential processing circuit (Runman™) and a computer, with a 12 bit analog-to-digital (A/D) converter board. The optical probe, which consists of a flexible rubber pad containing the halogen (four 20 W halogen bulbs) and tungsten (0.575 W) light sources and the pair of silicon photodetectors, is shown in Figure 1. The area of halogen light source is $2.1\times1.8\,\mathrm{cm}^2$, while the area of each silicon photodetector is $0.8\times2.1\,\mathrm{cm}^2$.[16] The tungsten light sources are significantly smaller in diameter

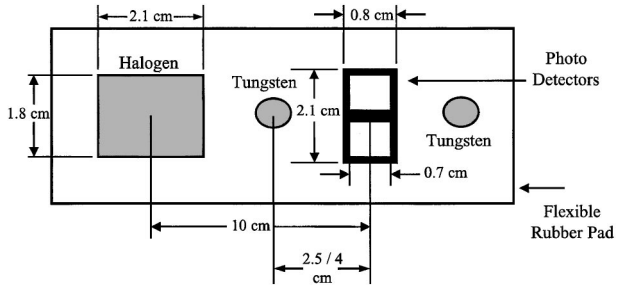

Fig. 1 The optical probe containing halogen and tungsten light sources and a pair of silicon photodetectors. S_1-D corresponds to a 10 cm source-detector separation, and S_2-D corresponds to a 2.5 cm source-detector separation.

than the halogen light source. The halogen light source is placed at a 10 cm separation from the detector (to achieve a penetration depth of ~4 cm in tissue). The two tungsten light sources are placed on either side of the detector at a 2.5 cm separation (to achieve a penetration depth of ~1 cm in tissue). The pair of silicon photodetectors receives time-shared, optical inputs from the tissue (which is illuminated alternately by the halogen and tungsten light sources) that are filtered at 760 and 850 nm by ±10 nm bandpass filters. The resulting electronic outputs at the two wavelengths are differentially amplified to provide their difference and sum at the two source-detector separations. The output is digitized using a 12 bit A/D board, integrated over a period of 2 s and then stored on a personal computer.

2.2 NIR Measurements of laboratory tissue phantoms

Two pairs of laboratory tissue phantoms were developed and evaluated for their effect on photon migration through the fetal head *in utero*. The first pair of tissue phantoms was used to study the effect of amniotic fluid between the maternal tissue and fetal head,[16] while the second pair of tissue phantoms was employed to investigate the effect of amniotic fluid that surrounds the fetal head.

2.2.1 *Model 1 and Model 2*

Figures 2(a) and 2(b) display a schematic of the first set of tissue phantoms, which consists of three glass containers representing the maternal tissue layer, which comprises the abdominal and uterine tissues (C), the amniotic fluid sac (B), and the fetal head (A). In Figure 2(a) (model 1) containers B and A are cylindrical, resulting in nonuniform contact between them, while in Figure 2(b) (model 2), containers B and A are rectangular, resulting in uniform contact between them. In each tissue phantom, the optical properties, i.e., the absorption and reduced scattering coefficients, were set using the solutions of India Ink and intralipid in water. The absorption and reduced scattering coefficients of the solution in container C were set at 0.08 cm^{-1} and 5 cm^{-1}, respectively, to simulate the averaged optical properties of fat and muscle tissues.[17] The absorption and reduced scattering coefficients of container A were set at $\mu_a=0.15\,\mathrm{cm}^{-1}$ and $\mu_s'=5\,\mathrm{cm}^{-1}$, respectively, to simulate the optical properties of the neonate brain.[18] Container B was filled with distilled water to simulate

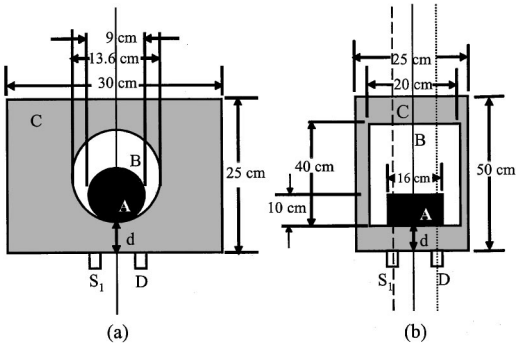

Fig. 2 A schematic of the first set of tissue phantoms, which consists of three glass containers representing the maternal tissue layer, which comprises the abdominal and uterine tissues (C), the amniotic fluid sac (B), and the fetal head (A). In Figure 2(a) (model 1), containers B and A are cylindrical, resulting in nonuniform contact between them, while in Figure 2(b) (model 2), containers B and A are rectangular, resulting in uniform contact between them. The absorption (μ_a) and reduced scattering coefficients (μ_s') are: 0.08 and 5 cm^{-1} for C, 0.02 and 0.1 cm^{-1} for B, and 0.15 and 5 cm^{-1}, for A, respectively. The fetal head depth is defined by *d*. S_1-D represents a 10 cm source-detector separation. The solid line represents the midline of S_1-D (midline position), the dashed line represents the midline of S_1 (source position) and the dotted line represents the midline of D (detector position).

the optical properties of amniotic fluid and was assumed to have absorption and reduced scattering coefficients of $\mu_a = 0.02\ cm^{-1}$ and $\mu_s' = 0.1\ cm^{-1}$, respectively.

2.2.2 *Model 3(a) and Model 3(b)*

Figures 3(a) and 3(b) display a second set of tissue phantoms. These tissue phantoms were developed to be similar to model 2, shown in Figure 2(b), because that tissue phantom, which has minimal intervening amniotic fluid between the maternal tissue and fetal head, best simulates the photon migration path through the fetal head *in utero*.[16] Note that the dimensions of containers, C, B, and A in the tissue phantoms, shown in Figures 3(a) and 3(b), are different from that of model 2, shown in Figure 2(b). In particular, the width of the fetal head is 10 cm, rather than 16 cm, since this more closely simulates

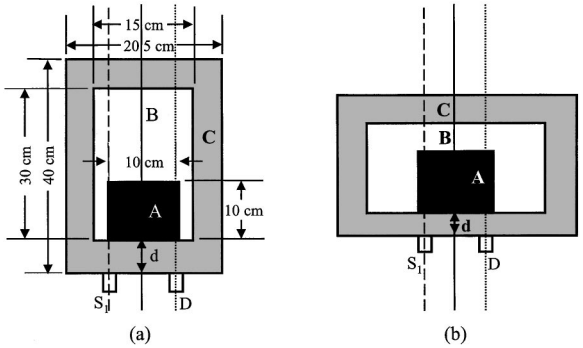

Fig. 3 A second set of tissue phantoms [based specifically on the optical properties and physical geometry of containers A, B, and C in model 2 [Figure 2(b)]]. The main difference between the tissue phantoms shown in Figures 3(a) [model 3(a)] and 3(b) [model 3(b)] is that model 3(b) has a larger area of amniotic fluid that surrounds the fetal head.

the actual dimensions of the late gestational fetal head *in utero*. The primary difference between the tissue phantoms shown in Figure 3(a) [model 3(a)] and Figure 3(b) [model 3(b)] is that model 3(b), has a larger area of amniotic fluid that surrounds the fetal head.

2.2.3 *NIR Measurements*

In Figures 2 and 3, the fetal head depth or synonymously, the maternal tissue thickness, is defined by ''*d*.'' ''S_1-D'' corresponds to a source-detector separation of 10 cm. The optical probe was attached to one of the walls of the outermost container C, such that the midline of S_1-D coincides with the midline of the tissue phantom (solid line). Container A was always kept in contact with container B to simulate the late gestational fetal head *in utero*. Containers B and A were displaced together to achieve different fetal head depths, *d*. Various fetal head positions were achieved by changing the position of container A, relative to that of the source-detector pair, S_1-D. The first position was achieved by positioning container A such that it was centered on the solid line, which represents the midline of S_1-D (midline position). The second position was achieved by positioning container A such that it was centered on the dashed line that represents the midline of S_1 (source position). The third position was achieved by positioning container A such that it was centered on the dotted line, which represents the midline of D (detector position).

NIR measurements at the 10 cm source-detector separation were made as a function of *d*, which was varied, from 2 to 4 cm (1–4 cm in the case of model 1), in 1 cm increments. Furthermore, these NIR measurements were performed for three different positions of container A (midline, source, and detector positions) relative to the optical probe.

2.3 Finite-difference simulations of the transport and diffusion equations

For each tissue phantom, corresponding numerical, finite-difference simulations based on the transport and diffusion equations were carried out. Photon migration in biological tissues can accurately be described by the time and energy independent equation of radiative transport, also known as the Boltzmann transport equation[19]

$$\Omega \cdot \nabla \psi(\mathbf{r},\Omega) + [\mu_a(\mathbf{r}) + \mu_s(\mathbf{r})]\psi(r,\Omega) = S(r,\Omega) + \mu_s(r) \int_{4\pi} \psi(r,\Omega') p(\Omega \cdot \Omega') dS . \quad (1)$$

Here $\mathbf{r}$ is the position vector and Ω is a unit vector pointing in the direction of photon propagation. $\Psi(r,\Omega)$ is the energy radiance in units of W cm^{-2} sr^{-1}. The source term $S(\mathbf{r},\Omega)$ represents power injected into a solid angle centered on Ω in a unit volume at $\mathbf{r}$. The absorption and scattering coefficients μ_a and μ_s are the inverse of the mean free path for absorption and scattering, respectively. The phase function $p(\Omega \cdot \Omega')$ describes the probability that during a scattering event, a photon with direction Ω' is scattered in the direction Ω.

The goal of an algorithm that solves Eq. (1) is to determine $\Psi(\mathbf{r},\Omega)$, or the derived parameter, $\phi(\mathbf{r})$, which is the energy fluence rate with the units of W cm^{-2}. The terms $\phi(\mathbf{r})$ can be written as

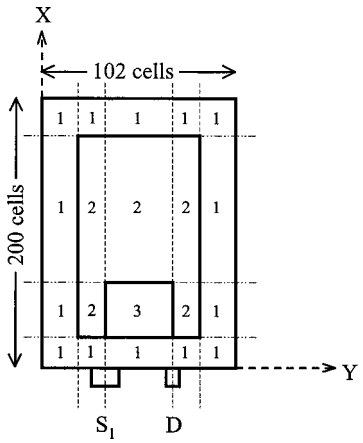

Fig. 4 A typical example of grid geometry for model 3(a) used for the assignment of absorption coefficient (μ_a) and reduced scattering coefficient (μ_s') in the different layers of the tissue phantoms. Specifically, the tissue phantom was divided into macro grids corresponding to maternal tissue (1), amniotic fluid (2), and the fetal head (3) in order to distinguish between μ_a and μ_s' of each layer. Furthermore, each macro grid was divided into uniform, orthogonal cells with a grid spacing of 0.2 cm, which corresponds to one reduced mean free path of scattering (inverse of μ_s').

$$\phi(\mathbf{r}) = \int_{4\pi} \psi(r,\Omega)\, d\Omega\,. \tag{2}$$

The solution of Eq. (1) is numerically determined using the finite-difference transport code called DANTSYS (Diffusion Accelerated Neutral Particle Transport Code System) that has originally been developed to calculate neutron transport in nuclear materials. Spatial discretization is performed by a diamond-differencing scheme, also called the Crank–Nicolson method.[20] For the discretization of the direction or angle, the method of discrete ordinates is employed.[21]

Another major feature of DANTSYS is the use of the diffusion synthetic acceleration (DSA) method for the iterative solution of the transport equation.[19,22] The method employs a corrected diffusion equation to accelerate the convergence of the transport iterations. Therefore, the first iteration provides a solution to the diffusion equation

$$-\{3[\mu_a+\mu_s']\}^{-1}\nabla^2\phi(r)+\mu_a\phi(r)=S(r)\,. \tag{3}$$

Notice that in Eq. (3), the scattering coefficient, μ_s has been replaced by the reduced scattering coefficient μ_s', which is defined as $\mu_s'=\mu_s(1-g)$, where g is the average of the cosine of the scattering angle, also called the anisotropy factor. The diffusion equation provides an approximation to the transport equation and can be used to accurately describe photon migration in media in which $\mu_s' \gg \mu_a$, and which does not contain strong variations in optical properties.[19] Because these criteria are fulfilled for many biological tissues, most researchers in biomedical optics use the simpler diffusion equation to model photon migration in tissues.

Forty eight angles were typically used for each two-dimensional simulation. Furthermore, the grid geometry shown in Figure 4 was used for the assignment of μ_a and μ_s' in the different layers of the tissue phantom. Specifically, the tissue phantom was divided into macro grids corresponding to maternal tissue, amniotic fluid, and the fetal head in order to distinguish between μ_a and μ_s' of each layer. Furthermore, each macro grid was divided into rectangular pixels with a grid spacing of 0.2 cm, which corresponds to one reduced mean free path of scattering ($\mathrm{mfp}'=1/\mu_s'$).

Table 1 For each numerical simulation, a two-dimensional image of the photon fluence in the tissue phantom was generated. This photon fluence image was employed to extract the total signal detected, R_{total}, calculate the visiting probability, P, for each cell in the photon fluence image, determine the fraction of detected photons that have visited the fetal head, F_{head}, and calculate the absolute target signal, R_{head}, originating from photons that have traveled through the fetal head. The table summarizes the relationship between the relevant variables.

Images	First Set of Derived Variables	Second set of Derived Variables
Photon Fluence	R_{total}	R_{head}
Visiting Probability, P	F_{head}	

The calculations for this study were performed on a CRAY Y-MP 8/128 platform. Computation time for a fully convergent transport solution ranged from several seconds to 30 min, depending on the size of the spatial mesh and the degree of angular discretization. Diffusion solutions (first iteration) were obtained in less than 1 s.

For each simulation, a two-dimensional image of the photon fluence in the tissue phantom was generated. This photon fluence image was employed to extract the total signal detected, R_{total}, calculate the visiting probability, P, for each cell in the photon fluence image, determine the fraction of detected photons that have visited the fetal head, F_{head}, and calculate the target signal detected from the fetal head, R_{head}. The variable R_{total} represents the photon fluence integrated over the cells at the detector end, relative to that integrated over the cells at the source end (the source strength of each cell is unity). The variable P is defined as the probability that a detected photon, originating from the source, has visited a particular cell in the tissue phantom. Numerically, visiting probability images can be obtained by pixel-wise multiplying two photon-fluence images for a particular source-detector configuration. The first photon fluence image is generated for the particular source position; the second photon fluence image is generated for the case in which the source position is now moved to where the detector is located. The variable F_{head} is calculated by taking the ratio of P, integrated over all the cells in the fetal head and P integrated over all the cells in the tissue phantom. Finally, the variable R_{head} is the product of R_{total} and F_{head}. Table 1 summarizes the order in which the relevant variables are calculated.

Numerical simulations of the tissue phantoms were performed for several source-detector separations, fetal head positions, and fetal head optical properties. For model 1 and model 2 shown in Figures 2(a) and 2(b), respectively, the photon fluence and visiting probabilities were calculated using both the transport and diffusion equations in order to select the appropriate numerical model for subsequent simula-

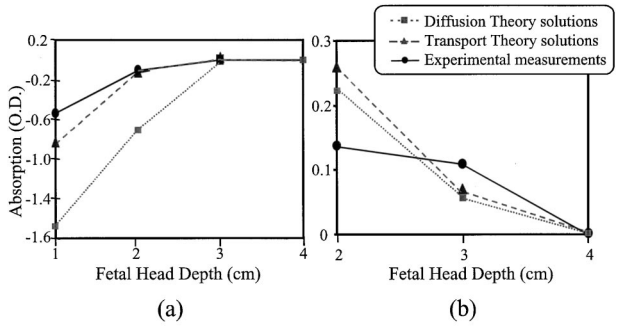

Fig. 5 Absorption as a function of fetal head depth obtained from numerical, finite-difference simulations of the transport and diffusion equations and from NIR measurements on the midline of model 1(a) and model 2(b) (see Figure 2), at a 10 cm source-detector separation.

tions. Note that the source and detector were approximated to be point sources for these two models. For model 3(a) and model 3(b) shown in Figures 3(a) and 3(b), respectively, only the transport equation was employed to calculate the photon fluence and visiting probabilities. In this case, the particular geometries of the sources and detectors as depicted in Figure 1 were adapted for the simulations.

3 Results and Discussion

3.1 Model 1 and Model 2

3.1.1 *Selection of the appropriate tissue phantom*

Figures 5(a) and 5(b) display the absorption as a function of fetal head depth obtained from the finite-difference simulations of the transport and diffusion equations and from NIR measurements on the midline of: (a) model 1 and (b) model 2, at a 10 cm source-detector separation. The absorption was calculated using Beer's law,[15] where the total signal detected, R_{total} at each fetal head depth was normalized relative to that at the largest fetal head depth (i.e., 4 cm), as at this depth, the accuracy of the NIR measurements is highest. We observed that at a small depth the influence of the glass-container walls becomes relatively stronger and the measurements are not as reproducible as for larger depth. In the simulations we did not account for the finite width of the container walls, which might explain the difference between the measured and calculated data at 2 cm. Furthermore, Figure 5(a) shows that the transport-equation-based simulations yield a better agreement with the experimental data than the diffusion-equation-based calculation. Overall, the computed and measured absorption versus fetal head depth shows similar trends for both model 1 and model 2. A comparison between model 1 and model 2 indicates that the absorption increases with fetal head depth, when there is nonuniform contact between the maternal tissue and fetal head; the opposite trend is observed when there is uniform contact between the maternal tissue and fetal head. The latter result should be expected here since the fetal head, which is relatively more absorbing than the maternal tissue, contributes progressively less to photon migration path, with increasing fetal head depth. A comparison of the absorption as a function of fetal head depth between that obtained from the tissue phantoms and that obtained from the maternal abdomen[15] indicates that the clinical results agree with tissue phantom results shown in Figure 5(b). Hence, model 2 more appropriately mimics the photon migration path through the fetal head *in utero*.

Figures 6(a)–6(d) display two-dimensional images of the photon fluence (a), (c) and visiting probability (b), (d) computed with the finite-difference algorithm based on the transport equation for (a), (b) model 1 and (c), (d) model 2. In model 1, the fetal head depth is 1 cm and in the case of model 2, the fetal head depth is 0.5 cm. An increase in the brightness corresponds to an increase in the photon fluence and an increase in the visiting probability. A comparison of the photon fluence images in Figures 6(a) and 6(c) indicates that the photon fluence in the region surrounding the fetal head is approximately one order of magnitude higher in model 1 [Figure 6(a)], relative to that in model 2 [Figure 6(c)]. Consequently, a comparison of the visiting probability images in Figures 6(b) and 6(d) indicates the visiting probability in the region surrounding the fetal head is about two orders of magnitude higher in model 1 [Figure 6(b)], relative to that in model 2 [Figure 6(d)].

The differences observed in the photon fluence and visiting probability images for model 1 and model 2 may be attributed to the effect of intervening amniotic fluid between the maternal tissue and fetal head in model 1, which contributes significantly to the photon migration path directly below the source. Evaluation of Figure 6(b) indicates that when there is nonuniform contact between the maternal tissue and fetal head, the intervening amniotic fluid diverts a large fraction of the photons around the fetal head, before they are detected at the surface. Because of the influence of low-absorbing amniotic fluid, the average absorption appears smaller. As the fetal head depth increases, the amniotic fluid will contribute progressively less to the photon migration path, while the stronger-absorbing maternal tissue will contribute more to the photon migration path. This will result in an increase in the average absorption with an increase in the fetal head depth, as is observed in Figure 5(a). Figure 6(d) shows that when there is uniform contact between the maternal tissue and fetal head, a large fraction of the photons migrate through the fetal head, before they are detected at the surface. As the fetal head depth increases, the fetal head will contribute progressively less to the photon migration path, and the less absorbing maternal tissue will contribute progressively more to the photon migration path. This will result in a decrease in the average absorption as a function of fetal head depth, as is observed in Figure 5(b). Since the NIR measurements made on the maternal abdomen agree with the tissue phantom results in Figure 5(b), it can be inferred that there is minimal intervening amniotic fluid between the maternal tissue and fetal head, in the case of the late gestational fetal head *in utero*.

3.1.2 *Selection of the appropriate numerical model: diffusion versus transport equation*

Figures 7(a) and 7(b) display the ratio of the photon fluence images computed with the finite-difference algorithms based on the diffusion and transport equations for model 1 and model 2, respectively. If this ratio equals 1 the photon fluences calculated from the diffusion and transport equations are equal. In the case of model 1 [Figure 7(a)], the ratio is

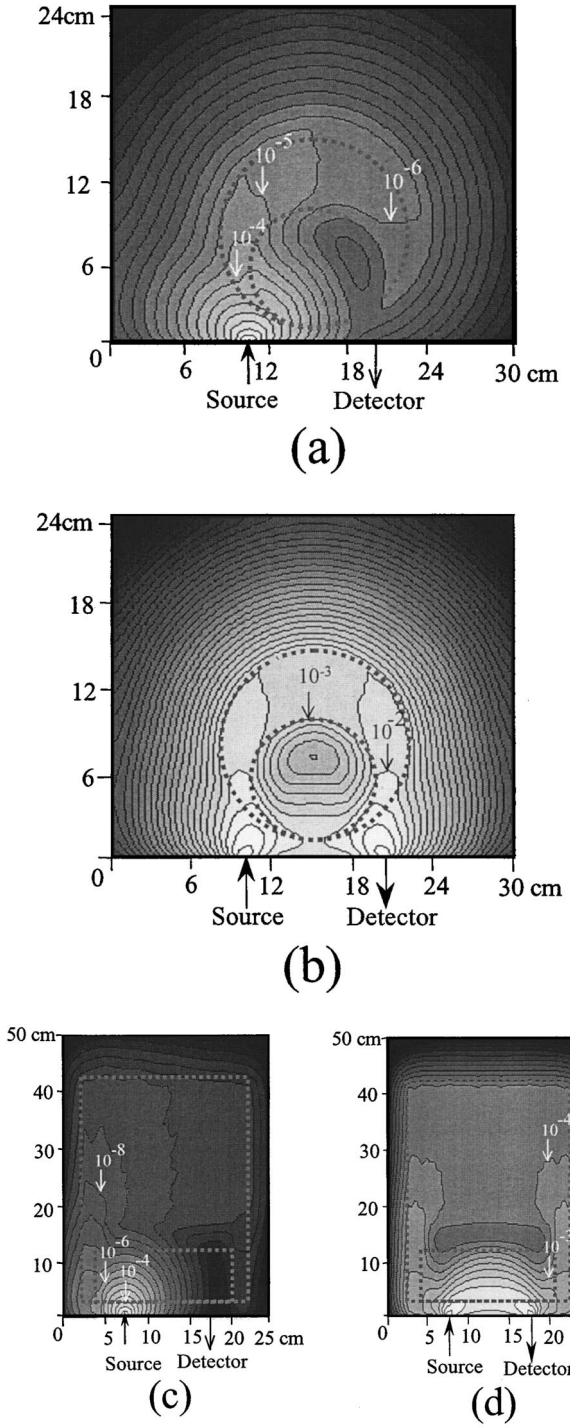

Fig. 6 Two-dimensional images of the (a), (c) photon fluence and (b), (d) visiting probability computed from finite-difference simulations of the transport equation for (a), (b) model 1 and (c), (d) model 2. In model 1, the fetal head depth is 1 cm and in model 2, the fetal head depth is 0.5 cm. An increase in the brightness corresponds to an increase in the photon fluence and an increase in the visiting probability.

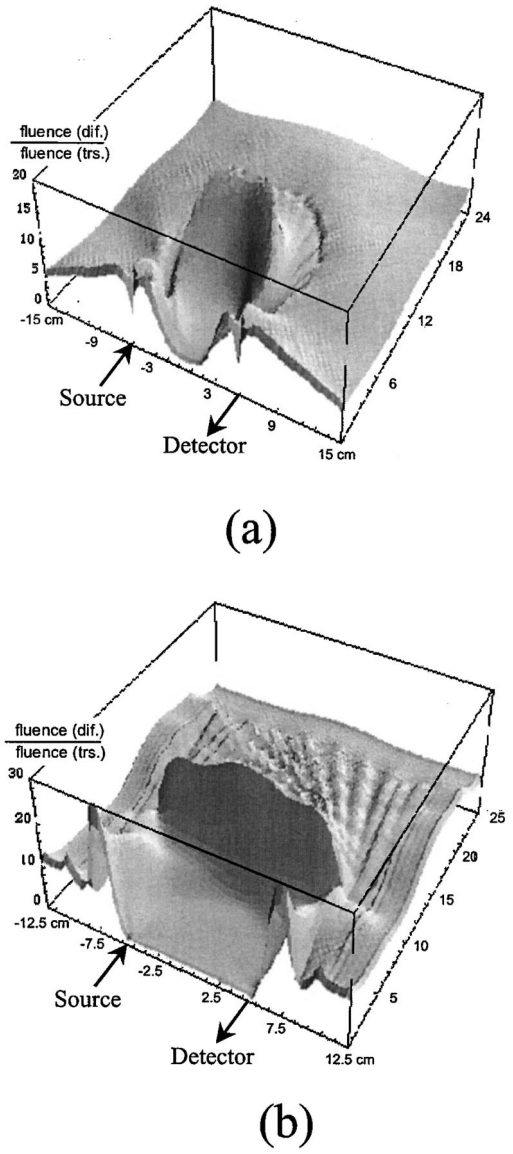

Fig. 7 The ratio of the photon fluence images computed from numerical simulations based on the diffusion and transport equations for (a) model 1 and (b) model 2. A ratio of one indicates that the photon fluences calculated from the diffusion and transport equations are the same.

significantly greater than unity in the region between the maternal tissue and fetal head, as well as behind the fetal head. This is attributed to the fact that the diffusion equation does not adequately describe photon migration in strongly heterogeneous media that contain areas with very low absorption and scattering, such as the amniotic fluid surrounding the fetal head.[19] In the case of model 2 [Figure 7(b)], the ratio is close to unity in the region between the maternal tissue and fetal head; it is significantly higher than unity only in the region behind the fetal head. This result shows that in the absence of the intervening amniotic fluid, the diffusion equation can be used to accurately predict the detector readings as long as the detector is located within the range of $-5\ \text{cm} < x < 5\ \text{cm}$. Since model 2 more appropriately mimics the photon migration path through the fetal head *in utero*, in which there is minimal intervening amniotic fluid between the maternal tissue and fetal head, simulations using either the diffusion or transport equations should yield similar results.

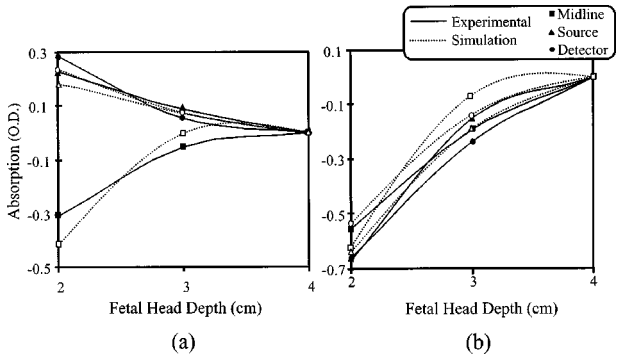

Fig. 8 Absorption as a function of fetal head depth obtained from numerical simulations based on the transport equation and from NIR measurements on: (a) model 3(a) and (b) model 3(b), at a 10 cm source-detector separation. In each case, absorption as a function of fetal head depth is shown for midline, source, and detector positions.

3.2 Models 3(a) and 3(b)

Figure 8 displays the absorption as a function of fetal head depth obtained from numerical simulations based on the equation of radiative transfer and from NIR measurements on model 3(a) [Figure 8(a)] and model 3(b) [Figure 8(b)]. The source and detector are separated by 10 cm (see Figure 1). In each case, the absorption as a function of fetal head depth is shown for midline, source, and detector positions. The absorption was calculated using Beer's law, where the total signal detected, R_{total} at each fetal head depth was normalized relative to that at the largest fetal head depth of 4 cm. Note that for all three fetal head positions the experimental measurements and the computer simulations are comparable to each other. An even better modeling correlation with experimental results may be obtained if we take the finite thickness of containers into account during the numerical simulations.

Evaluation of Figure 8(a) indicates that the absorption increases with fetal head depth, when the fetal head is directly below the midline. However, the absorption decreases with increasing fetal head depth when the fetal head is directly below the source or the detector. Figure 8(b) shows that the absorption increases as a function of fetal head depth for all three fetal head positions. The increase in absorption with increasing fetal head depth in these cases may be attributed to the effect of amniotic fluid surrounding the fetal head, rather than that intervening between the maternal tissue and fetal head as was observed previously in Figure 5(a). A comparison of the absorption as a function of fetal head depth between that obtained from the tissue phantoms and that obtained from the maternal abdomen[15] indicates that the clinical results agree with tissue phantom results shown in Figure 8(a). This is true particularly for the case in which the fetal head is directly below the source or directly below the detector. Hence, model 3(a), rather than model 3(b), more appropriately mimics the photon migration path through the fetal head *in utero*. It can be inferred that in the case of the late gestational fetal head *in utero*, the intervening amniotic fluid between the maternal tissue and fetal head and the amniotic fluid surrounding the fetal head have a minimal effect on photon migration through the fetal head *in utero*.

3.2.1 *Estimation of photon migration through the fetal head in utero*

Table 2 compares the total signal detected, R_{total}, the fraction of detected photons that have visited the fetal head, F_{head}, and the target signal detected, R_{head}, for models 3(a) and 3(b) as calculated with the finite-difference algorithm. The source-detector separation is 10 cm. Results are shown for a head positioned below the midline, source, and detector, respectively. The fetal head depth is 3 cm, which is the upper limit of fetal head depths observed in near-term patients.

It can be seen that for models 3(a) and 3(b), the total detect signal R_{total} is seven orders of magnitude lower than the source strength. For model 3(a), R_{total} is highest when the fetal head is directly below the midline. F_{head} ranges from 4%–6% and is highest when the fetal head is directly below the source. We find that R_{head} is highest when the fetal head is directly below the source. Results for model 3(b) indicate that R_{total} is highest when the fetal head is directly below source. F_{head} ranges from 3%–7% and is highest when the fetal head is directly below the source. It follows that R_{head} is highest (6.01×10^{-8} W cm^{-2}) when the fetal head is directly below the source. It may be inferred from these results that maximal sensitivity to the fetal head can be achieved if the optical

Table 2 The total signal detected, R_{total}, the fraction of detected photons that have visited the fetal head, F_{head}, and the target signal detected, R_{head}, calculated with the transport-equation algorithm. For these simulations models 3(a) and 3(b) are used, and the source-detector (S-D) separation is 10 cm. In all cases the fetal head depth is 3 cm (upper limit of fetal head depths observed in near-term patients). Results are shown for the three situations in which the head is positioned directly below the midline, below the source, and below the detector.

Fetal head position (S-D=10 cm)	Model 3(a)			Model 3(b)		
	$R_{\text{total}}\times10^{-7}$ (W cm^{-2})	F_{head} (%)	$R_{\text{head}}\times10^{-8}$ (W cm^{-2})	$R_{\text{total}}\times10^{-7}$ (W cm^{-2})	F_{head} (%)	$R_{\text{head}}\times10^{-8}$ (W cm^{-2})
Midline	5.28	4.23	2.23	6.20	3.4	2.11
Source	4.51	5.63	2.54	9.07	6.63	6.01
Detector	4.36	5.20	2.26	7.71	6.49	5.00

Table 3 R_{total}, F_{head}, and R_{head} from numerical simulations of the transport equation at a 7 cm source-detector (S-D) separation, for model 3(a). Specifically, these parameters were computed for fetal head depths of 3 cm (upper limit observed in near-term patients), 2.2 cm (average observed in near-term patients) and 1.4 cm (lower limit observed in near-term patients). The fetal head is positioned directly below the source.

Fetal head depth (cm) S-D=7 cm	$R_{total}\times10^{-5}$ (W cm^{-2})	F_{head} (%)	$R_{head}\times10^{-6}$ (W cm^{-2})
1.4	0.97	28.29	2.74
2.2	1.65	8.60	1.42
3.0	2.10	2.59	0.54

Table 4 Percent decrease in R_{total} for a 20% increase of μ_a (from 0.15 to 0.18 cm^{-1}) in the fetal head, as calculated with the transport-theory-based algorithm assuming model 3(a). The source-detector separation (S-D) is 7 cm. The change in μ_a, from 0.15 to 0.18 cm^{-1} (at a wavelength of 780 nm) corresponds to a change in blood saturation, from 70% to 35%, at a fixed blood volume of 0.35 mM (4% of tissue volume).

Fetal head depth (cm) S-D=7 cm	Percent decrease in R_{total} (W cm^{-2}) for a 20% increase in the absorption coefficient in the fetal head (%)
1.4	24.17
2.2	9.09
3.0	2.38

probe is positioned on the maternal abdomen such that the fetal head is directly below the source.

Table 3 shows computed R_{total}, F_{head}, and R_{head} values for three different fetal head depths, 3 cm (upper limit observed in near-term patients), 2.2 cm (average observed in near-term patients), and 1.4 cm (lower limit observed in near-term patients). Calculations were performed using the discrete-ordinate transport codes. For these simulations, model 3(a) is used with the fetal head located directly below the source. The source-detector separation is 7 cm.

As expected, the table shows that increasing the fetal head depths from 1.4 to 3.0 cm leads to an increase in the total signal detected R_{total}. The relatively higher absorbing head intersects less and less of the photons traveling from the source to the detector. This is also reflected in the decrease of the relative contribution of photons that traveled through the head to the overall signal: $F_{head}=100R_{head}/R_{total}$ drops from 28.29% at 1.4 cm depth to only 2.59% at 3.0 cm depth.

Comparing $R_{total}=2.10\times10^{-5}$ W cm^{-2} for 7 cm source-detector separation (Table 3) and $R_{total}=4.51\times10^{-7}$ W cm^{-2} for 10 cm (Table 2) source-detector separation, for the same fetal head depth and position, shows that at 7 cm separation, R_{total} is two orders of magnitude higher. On the other hand, at 7 cm source-detector separation $F_{head}=2.10\%$ is only a factor of 2 lower than $F_{head}=5.63\%$ at 10 cm source-detector separation. Hence, R_{head}, which represents the signal detected from the fetal head, is more than 21 times higher at 7 cm source-detector separation ($R_{head}=0.54\times10^{-6}$ W cm^{-2}) than at the 10 cm source-detector separation ($R_{head}=2.54\times10^{-8}$ W cm^{-2}). Therefore, reducing the source-detector separation from 10 to 7 cm dramatically increases the number of detected photons coming from the fetal head, while only slightly affecting the sensitivity represented by F_{head}. While a further decrease of the source-detector separation will further increase R_{total} and R_{head}, the sensitivity F_{head} fast approaches the noise floor of the measurement device. In other words, once F_{head} is smaller than the noise level in the measurement, a further increase in the absolute number of photons from the head is no longer beneficial.

To determine if R_{head} at a 7 cm source-detector separation can be measured with the currently available NIR technology, let us consider an example in which the maternal abdomen is illuminated with a 1 mW laser diode at 800 nm (within the specifications of available laser diodes). In this example, about 10^{15} photons/s from the light source are launched into the maternal abdomen. Based on the values of R_{head} in Table 3, the number of detected photons that have visited the fetal head will be approximately six to seven orders of magnitude lower. Therefore, 10^8-10^9 photons that have visited the fetal head will reach the detector. This number of photons can easily be measured with the currently available NIR technology.[23] However, these photons reach the detector together with 38 times (considering the upper limit of fetal head depth) as many photons from other locations to constitute the total signal detected, R_{total}. Therefore, in order to distinguish the R_{head} from R_{total} and the noise floor of the system, the instrument employed must have the signal to noise ratio at least greater than 38. Our current system has a signal to noise ratio of at least 100:1.

To further evaluate the feasibility of monitoring changes in blood oxygenation in the fetal head by trans-abdominal measurements, we investigated the changes in R_{total} as a function of changes in the blood saturation. Assuming that 4% of the fetal head tissue volume is filled with blood, we obtain a whole blood concentration of 0.35 mM. For this case, a change in blood saturation from 70% to 35% leads to a 20% change in the absorption coefficient of the fetal head from $\mu_a=0.15$ cm^{-1} to $\mu_a=0.18$ cm^{-1}, at a wavelength of 780 nm. Using these numbers and the geometry of model 3(a), we employed the discrete-ordinate transport code to calculate the changes in R_{total} at a source-detector separation of 7 cm. In these simulations, the optical properties of the maternal tissue layer were fixed. Table 4 displays the results. As can be seen, a 20% increase of μ_a (from $\mu_a=0.15$ to $\mu_a=0.18$ cm^{-1}) in the fetal head at a depth of 1.4 cm, leads to a decrease in the total detected signal R_{total} of 24.17%. As expected, as the fetal head depth increases the change in R_{total} decreases. At 3 cm depth the signal only changes by 2.38%. Therefore, while it will be easy to detect changes in blood saturation when the fetal head is only 1.4 cm deep, at 3 cm depth the signal to noise ratio should be at least 100:1. In case other factors vary at the same time, for example, the optical properties of the overlaying maternal tissue may change, even more sensitive measurements will be essential. For deep fetal heads it furthermore may be necessary to perform measurements with multiple source-detector pairs and to employ appropriate

three-dimensional reconstruction algorithms to accurately monitor changes in blood volume and blood oxygenation.

4 Summary

In this work, we developed laboratory tissue phantoms that are complex enough to be congruent with the major clinical findings, yet simple enough to allow easy manipulation of various tissue and geometry parameters. Experimental results from measurements on these phantoms were compared to calculations that were based on numerical solution to the equation of radiative transfer and the diffusion equation.

Our results indicate that, a simple two-layer tissue phantom, which consists of a maternal tissue layer on top of the fetal head, best mimics the optical properties and physical geometry of the photon migration path through the fetal head *in utero*. Models that assume low-absorbing and low-scattering amniotic fluid in the photon path do not yield results in agreement with clinical findings.

In accordance with previous studies,[19] we found large differences between diffusion-theory-based and transport-theory-based simulations in low-absorbing and low-scattering regions of the medium. Therefore, a numerical model based on the transport equation is necessary to simulate photon migration through the fetal head *in utero*, in the case when there is intervening amniotic fluid. However, as our studies show the effect of amniotic fluid is minimal in the case of the late gestational fetal head *in utero*, therefore numerical simulations using the simpler diffusion equation should suffice to accurately predict the detector readings in this particular case.

Furthermore, the numerical simulations and NIR measurements on tissue phantoms showed that the sensitivity of the optical probe to the fetal head is maximized, when the probe is placed on the maternal abdomen, such that the source is directly above the fetal head. This is corroborated by the NIR measurements made on the maternal abdomen in a clinical setting.[15] Moreover, our theoretical studies revealed that as the source-detector separation is reduced from 10 to 7 cm the absolute number of photons detected R_{head} that have traveled through the fetal head is drastically increased. At the same time, the ratio F_{head} of the photons coming from the head as compared to all the photons detected decreases only slowly. Further decreasing the source detector separation will further increase the absolute number of photons detected, R_{head} that have traveled through the fetal head. However, the parameter F_{head} has to stay larger than the signal to noise ratio of the measurement in order to make use of a large R_{head} value.

Several improvements of the developed phantoms may be considered for future studies. Currently the maternal layer is considered homogeneous. A model that realizes a composite maternal layer consisting of fat and muscle tissue may lead to even better agreement between phantom and clinical studies. To study clinical scenarios of prematurity, models have to be tested that use smaller fetal heads and have more intervening amniotic fluid. In these cases, the optical properties of the amniotic fluid, which is currently represented by distilled water, may be varied to simulate clinically relevant cases in which blood or scattering particles are present (e.g., placenta previa, abruptio placenta, and chorioamnionitis[24–26]). Finally, studies that use multiple source-detector pairs and employ three-dimensional tomographic reconstruction techniques should further elucidate the potential and limits of quantitative, trans-abdominal, NIR imaging.

Acknowledgments

This research project is funded in part by the National Institutes of Health (Grant No. 1R43HL61057-06) and the City of New York Council Speaker's Fund for Biomedical Research: Toward the Science of Patient Care.

References

1. M. M. Adams, ''The continuing challenge of pre-term delivery,'' *J. Am. Med. Assoc.* **273**(2), 739–740 (1995).
2. K. B. Nelson and J. H. Ellenberg, ''Antecedents of cerebral palsy: Multivariate analysis of risk,'' *New. Engl. J. Med.* **315**(2), 81–86 (1986).
3. C. P. Torfs, B. van den Berg, F. W. Oechsli, and S. Cummins, ''Prenatal and perinatal factors in the etiology of cerebral palsy (see comments),'' *J. Pediatr. (St. Louis)* **116**, 615–619 (1990).
4. J. Lavery, ''Nonstress fetal heart rate testing,'' *Clin. Obstet. Gynecol.* **25**, 689 (1982).
5. F. A. Manning, C. R. Harman, and I. Morrison, ''Fetal assessment based on fetal biophysical profile scoring,'' *Am. J. Obstet. Gynecol.* **162**, 3 (1990).
6. B. Chance, ''Optical method,'' *Annu. Rev. Biophys. Chem.* **20**, 1–28 (1991).
7. B. Chance, M. Cope, B. Dugan, N. Ramanujam, and B. Tromberg, ''Phase measurements of absorbers and scatterers in tissue: Review,'' *Rev. Sci. Instrum.* **69**, 3457–3481 (1998).
8. M. S. Patterson, B. Chance, and B. C. Wilson, ''Time resolved reflectance and transmittance for the measurement of tissue optical properties,'' *Appl. Opt.* **28**, 2331–2336 (1989).
9. M. S. Patterson, J. D. Moulton, B. C. Wilson, K. W. Berndt, and J. R. Lakowicz, ''Frequency domain reflectance for the determination of the scattering and absorption properties of tissue,'' *Appl. Opt.* **30**, 4474–4476 (1991).
10. W. M. Armstead and C. D. Kurth, ''Different cerebral hemodynamic responses following fluid percussion brain injury in the newborn and juvenile pig,'' *J. Neurotrauma* **11**, 487–97 (1994).
11. V. Quaresima, R. Springett, M. Cope, J. T. Wyatt, D. T. Delpy, M. Ferrari, and C. E. Cooper, ''Oxidation and reduction of cytochrome oxidase in the neonatal brain observed by *in vivo* near-infrared spectroscopy,'' *Biochim. Biophys. Acta* **1366**, 291–300 (1998).
12. H. Y. Ma, Q. Xu, J. R. Ballesteros, and B. Chance, ''Quantitative study of hypoxia stress in piglet brain by a two-wavelength IQ phase modulation oximeter,'' *Proc. SPIE* **3597**, 642–649 (1999).
13. L. Skov, ''Noninvasive brain monitoring with near infrared spectroscopy in newborn infants,'' *Dan. Med. Bull.* **43**, 277–284 (1996).
14. D. A. Benaron, C. D. Kurth, J. M. Steven, M. Delivoria-Papadopoulos, and B. Chance, ''Transcranial optical path length in infants by near-infrared phase-shift spectroscopy,'' *J. Clin. Monit.* **11**, 109–117 (1995).
15. N. Ramanujam, G. Vishnoi, A. H. Hielscher, M. E. Rode, I. Forouzan, and B. Chance, ''Photon migration through the fetal head *in utero* using continuous wave, near infrared spectroscopy: Clinical and experimental model studies,'' in this issue.
16. G. Vishnoi, A. H. Hielscher, N. Ramanujam, and B. Chance, ''Tissue phantom studies on photon migration through fetal brain *in utero* using near infra-red spectroscopy,'' *Proc. SPIE* **3597**, 650–660 (1999).
17. J. B. Fishkin, C. Coquoz, E. R. Anderson, M. Brenner, and B. J. Tromberg, ''Frequency domain photon migration measurements of normal and malignant tissue optical properties,'' *Appl. Opt.* **36**, 10–19 (1997).
18. E. Okada, M. Firbank, M. Schweiger, S. R. Arridge, M. Cope, and D. T. Delpy, ''Theoretical and experimental investigation of NIR light propagation in a model of adult head,'' *Appl. Opt.* **36**, 21–31 (1997).
19. A. H. Hielscher, R. E. Alcouffe, and R. L. Barbour, ''Comparison of finite-difference transport and diffusion calculations for photon migration in homogeneous and heterogeneous tissues,'' *Phys. Med. Biol.* **43**, 1285–1302 (1998).
20. R. E. Alcouffe, ''An adaptive weighted diamond differencing method

for three-dimensional xyz geometry,'' *Trans. Am. Nucl. Soc.* **68**, Part A, 206–212 (1993).
21. B. G. Carlson and K. D. Lathrop, ''Transport Theory,'' in *The Method of Discrete Ordinates Computational Methods in Reactor Physics*, H. Greenspan, C. Kelber, and D. Okrent, Eds., pp. 171–270, Gordon and Breach, New York (1968).
22. R. E. Alcouffe, R. S. Baker, F. W. Brinkley, D. R. Marr, R. D. O'Dell, and W. F. Walters, *DANTSYS: A diffusion accelerated neutral particle transport code system*, Los Alamos National Laboratory, Los Alamos, New Mexico, Manual LA-12969-M (1995).
23. B. Chance, M. Cope, B. Dugan, N. Ramanujam, B. Tromberg, ''Phase measurements of absorbers and scatterers in tissue: Review,'' *Rev. Sci. Instrum.* **69**, 3457–3481 (1998).
24. J. M. Perlman and R. Risser, ''Severe fetal acidemia: Neonatal neurologic features and short-term outcome,'' *Pediatr. Neurol.* **9**(4), 277–282 (1993).
25. J. M. Perlman and R. Risser, ''Can asphyxiated infants at risk for neonatal seizures be rapidly identified by current high-risk markers?'' *Pediatrics* **97**(4), 456–462 (1996).
26. T. M. O'Shea, K. L. Klinepeter, P. J. Meis, and R. G. Dillard, ''Intrauterine infection and the risk of cerebral palsy in very low-birthweight infants,'' *Pediatr. Perinat. Epidemiol.* **12**(1), 72–83 (1998).